

## Article

# Intelligent Controlled DSTATCOM for Power Quality Enhancement

Jun-Hao Chen <sup>1,\*</sup>, Kuang-Hsiung Tan <sup>1</sup> and Yih-Der Lee <sup>2</sup>

<sup>1</sup> Department of Electrical and Electronic Engineering, Chung Cheng Institute of Technology, National Defense University, Taoyuan 335, Taiwan; s913115@gmail.com

<sup>2</sup> Nuclear Instrumentation Division, Institute of Nuclear Energy Research, Taoyuan 325, Taiwan; ydlee@iner.gov.tw

\* Correspondence: ru6auu4@gmail.com; Tel.: +886-3-380-0301 (ext. 128)

**Abstract:** In this study, a three-phase four-wire distribution static compensator (DSTATCOM) is proposed to improve power quality, including the compensation of the three-phase unbalanced grid currents, the total harmonic distortion (THD) reduction of the grid current, and the power factor (PF) correction. Moreover, when different types of loads vary in the power system, the instantaneous power follows into or out of the DC-link capacitor in the DSTATCOM and results in poor transient responses of the grid current and DC-link voltage and performance deterioration. Hence, the DC-link voltage control plays a significant part in the DSTATCOM under load variation. For the purpose of mending the transient responses of the grid currents and DC-link voltage control and the performance of the DSTATCOM, the conventional proportional-integral (PI) controller is substituted with a novel online trained wavelet Takagi-Sugeno-Kang fuzzy neural network (WTSKFNN) controller in this study. Furthermore, the network structure and the online learning method of the proposed WTSKFNN controller are described in detail. Finally, the experimental results are given to certify the feasibility and effectiveness of the DSTATCOM using the proposed WTSKFNN controller for the power quality enhancement and the DC-link control improvement under load variation.

**Keywords:** DSTATCOM; power quality; THD; power factor; wavelet theory; fuzzy neural network



**Citation:** Chen, J.-H.; Tan, K.-H.; Lee, Y.-D. Intelligent Controlled DSTATCOM for Power Quality Enhancement. *Energies* **2022**, *15*, 4017. <https://doi.org/10.3390/en15114017>

Academic Editors: Cheng-I Chen and Yeong-Chin Chen

Received: 3 May 2022

Accepted: 28 May 2022

Published: 30 May 2022

**Publisher's Note:** MDPI stays neutral with regard to jurisdictional claims in published maps and institutional affiliations.



**Copyright:** © 2022 by the authors. Licensee MDPI, Basel, Switzerland. This article is an open access article distributed under the terms and conditions of the Creative Commons Attribution (CC BY) license (<https://creativecommons.org/licenses/by/4.0/>).

## 1. Introduction

Nowadays, owing to the growing penetration rate of the renewable energy sources connected with the utility grid, the power quality issue has become a significant challenge resulting from inherent intermittency and uncertainty [1–3]. In other words, the increasing renewable energy sources may lead to the unbalanced grid current, uncontrolled reactive power, voltage variations, and flickers [1,2]. Moreover, owing to the widespread utilization of the sensitive apparatus in medical facilities, commercial, and industrial applications such as x-ray machine, computers, rectifier, switched mode power supplies, transformer, arc furnaces, and so on, the power quality deterioration seriously occurs and includes a high reactive power burden, load unbalance, harmonic currents, lagging power factor (PF), etc., [4–7].

One of the proper methods to mend power quality is the distribution static compensator (DSTATCOM). The main functions of the DSTATCOM are to achieve the harmonic suppression, reactive power compensation, PF correction, and load balancing in the power system [8,9]. In terms of the control algorithms, the DSTATCOM is generally classified into two categories: (1) instantaneous reactive power (IRP) theory, and (2) the synchronous reference frame (SRF) method [10,11]. The IRP theory is implemented in the  $\alpha\beta$  stationary reference frame and calculates the instantaneous power of the loads in the stationary reference frame. Hence, the IRP theory is also named  $pq$  theory. Though the IRP theory is simple without the phase-locked loop (PLL), the calculation of instantaneous power using the IRP theory may not obtain the accurate power phenomena in a three-phase unbalanced

system [12]. On the other hand, since the SRF method is performed in the  $dq0$  rotating reference frame, the SRF method is also named the  $dq$  method. Due to higher accuracy than the stationary reference frame-based technique, the SRF method is widely adopted in the DSTATCOM [13,14]. Thus, much research using the DSTATCOM has been proposed for power quality improvement [15–17]. In [15], an online strategy for DSTATCOM using secondary controls in a microgrid was proposed. In [16], a grid-connected photovoltaic system using DSTATCOM was proposed for power quality enrichment. Furthermore, an adaptive technology of the DSTATCOM was developed to mend the power quality [17]. In addition, since the DC-link capacitor is connected at the DC side of the DSTATCOM, the DC-link capacitor is considered an energy buffer for DSTATCOM to generate the injection or mitigation current to the source current [14]. However, when the load varies, the instantaneous power follows into or out of the DC-link capacitor in the DSTATCOM, resulting in the poor transient responses of the grid currents and DC-link voltage and performance deterioration. Hence, the DC-link voltage control to maintain the constant voltage level under load variation plays a significant part in the DSTATCOM [4,14,18].

Owing to the easy implementation and simple structure of the proportional-integral (PI) controller, the PI controller has been extensively used in industrial application [19]. Nevertheless, some demerits of the PI controller, such as poor disturbance rejection, seriously affects the performance of the control system [19,20]. In other words, since the designed parameters of the PI controller are only for the assumed condition, the performance of the PI-based control system will be decreased in the case of the external interference and disturbances such as sudden load change [19,20]. Thus, intelligent control to cope with the applications of knowledge bases, expert systems, and fuzzy neural network (FNN) for complicated control problems have been proposed in recent years. The wavelet fuzzy neural network (WFNN) is one of the intelligent control methods. Since the WFNN is composed of the FNN and wavelet neural network (WNN), the WFNN has the following merits [21–23]: (1) the decomposition property of the wavelet theory; (2) the high precision with the reduced network size of the WNN; (3) the abilities of WNN in learning and converging quickly; (4) the ability of fuzzy reasoning to deal with uncertain information; (5) the advantage of the FNN without a mathematic model and (6) the ability to approximate nonlinear systems and uncertainties. Hence, the WFNN intelligent control has been investigated in different applications. In [24], the low-voltage ride through performance for the weak grid condition is improved by a photovoltaic system using recurrent WFNN. In [25], an adaptive self-constructing WFNN was adopted to achieve the superior dynamic function of the high-speed permanent magnet synchronous motor drive. A recurrent Petri WFNN for the voltage restoration control of storage systems to provide fast control response was proposed in [26]. Moreover, due to the interpretability and universal approximation capability, the Takagi-Sugeno-Kang (TSK) fuzzy control has been successfully adopted in extensive fields, including pattern recognition, data mining, classification, and system controls [27–29]. The main principle of the TSK fuzzy control is that the input space can be decomposed into fuzzy regions. Furthermore, the system can be approximated in every region by the meaning of an uncomplicated model [27]. Hence, the TSK fuzzy system owns the ability to effectively represent a highly nonlinear system using a small number of rules [29]. Recently, much literature using the TSK fuzzy system has been proposed [30,31]. A TSK-type FNN to estimate the lumped uncertainty of a six-phase, permanent-magnet, synchronous motor drive system was proposed in [30]. In [31], a TSK fuzzy system using the semi-supervised learning method was proposed for data with label noise. Consequently, owing to the merits of the WFNN and TSK fuzzy control, a novel online trained wavelet Takagi-Sugeno-Kang fuzzy neural network (WTSKFNN) controller is firstly developed to supersede the conventional PI controller in the DSTATCOM.

In this study, a three-phase four-wire voltage source converter (VSC)-based DSTATCOM using the SRF method is proposed to enhance power quality, including compensation of the three-phase unbalanced grid currents, total harmonic distortion (THD) reduction of the grid current, and the PF correction. Moreover, since the different types of loads

vary in power systems, resulting in the poor transient response of the grid currents and DC-link voltage and the performance deterioration of the DSTATCOM, the conventional PI controller is substituted with the proposed WTSKFNN controller for the DC-link voltage control to mend the transient response of the DSTATCOM in this study. The detailed control theory of the DSTATCOM is introduced in Section 2. Furthermore, the network structure and online learning of the proposed WTSKFNN controller are described in Section 3. The experimental results using the WTSKFNN controlled DSTATCOM to enhance the power quality are demonstrated in Section 4. Finally, some conclusions will be depicted in Section 5.

### 2. Three-Phase Four-Wire DSTATCOM

In this study, the schematic diagram of the three-phase four-wire VSC-based DSTATCOM is illustrated in Figure 1. The DSTATCOM is connected with the utility grid, nonlinear load, and the unbalanced inductive load via the interfacing inductor in parallel. The DC side of the DSTATCOM is equipped with a DC-link capacitor  $C_{dc}$ . Moreover, the ripple filter with common neutral point N is also connected with DSTATCOM in parallel to smoothen the compensation currents  $i_{Fa}$ ,  $i_{Fb}$ ,  $i_{Fc}$  of the DSTATCOM [10]. The main objective of the compensation currents  $i_{Fa}$ ,  $i_{Fb}$ ,  $i_{Fc}$  are to suppress the current harmonics and unbalanced currents of the utility grid and to compensate the reactive power for maintaining the unity PF at utility grid [6]. The fourth wire of the DSTATCOM is adopted to repress the neutral current. The relationship of the four-wire currents of the DSTATCOM can be represented in the following:

$$i_{Fn} = i_{Fa} + i_{Fb} + i_{Fc} \tag{1}$$

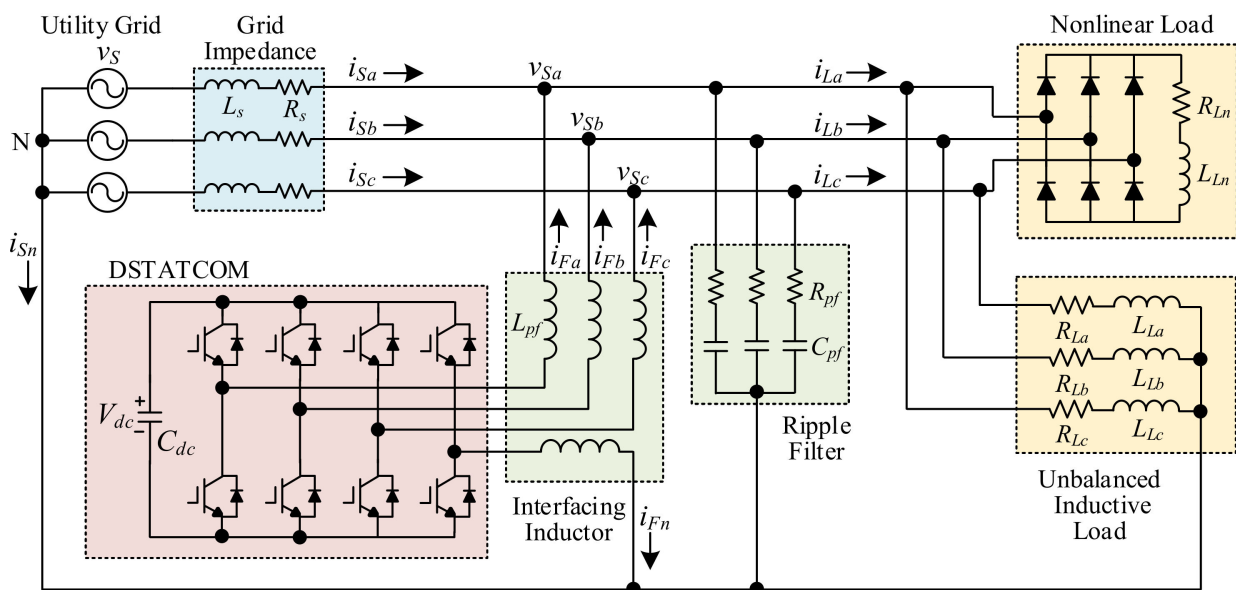


**Figure 1.** Schematic diagram of three-phase four-wire VSC-based DSTATCOM with nonlinear and unbalanced inductive loads.

The frequency and line to line voltage  $v_S$  of the utility grid are 60 Hz and 220 Vrms, respectively. In addition, the control block diagram of the DSTATCOM is presented in Figure 2. Firstly, the three-phase voltages  $v_{Sa}$ ,  $v_{Sb}$ ,  $v_{Sc}$  of the utility grid are detected and perform the PLL algorithm for acquiring the electrical angle  $\theta_e$ . The voltage amplitude  $V_m$  can be calculated by the following equation [6,9]:

$$V_m = \sqrt{\frac{2}{3}(v_{Sa}^2 + v_{Sb}^2 + v_{Sc}^2)} \tag{2}$$

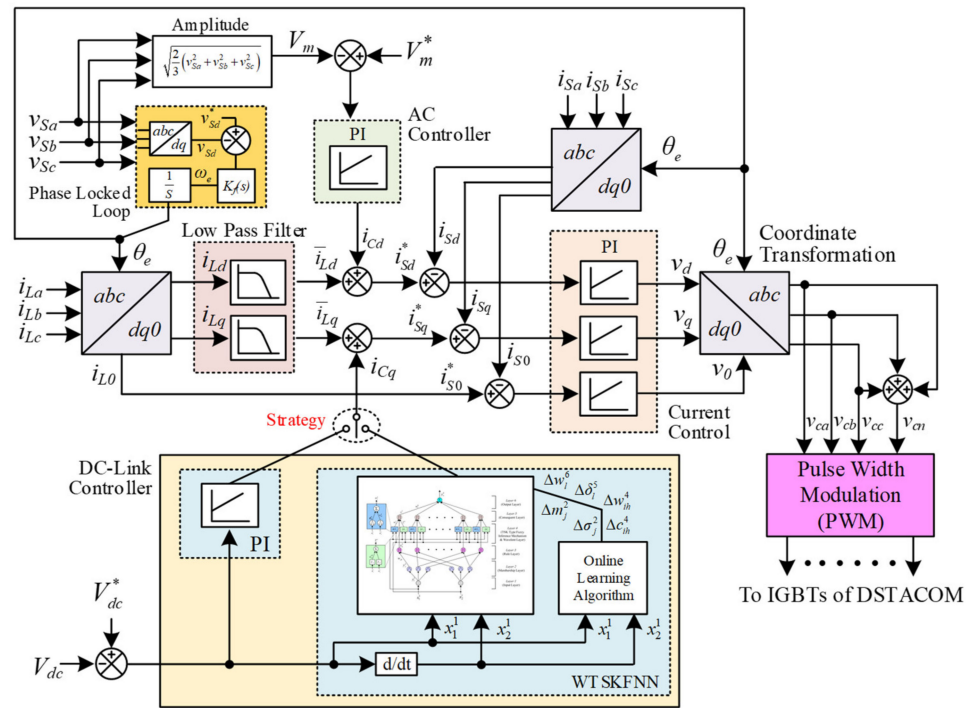


Figure 2. Control block diagram of DSTATCOM.

The difference between the amplitude command  $V_m^* = 180V$  and the voltage amplitude  $V_m$  is transmitted to the AC controller, namely the PI controller, for generating the control current  $i_{Cd}$ . In addition, the three-phase load currents  $i_{La}$ ,  $i_{Lb}$ ,  $i_{Lc}$  are detected to compute the  $dq0$ -axis currents  $i_{Ld}$ ,  $i_{Lq}$  and  $i_{L0}$  via the  $abc/dq0$  coordinate transformation as follows:

$$\begin{bmatrix} i_{Ld} \\ i_{Lq} \\ i_{L0} \end{bmatrix} = \frac{2}{3} \begin{bmatrix} \cos \theta_e & \cos(\theta_e - \frac{2\pi}{3}) & \cos(\theta_e + \frac{2\pi}{3}) \\ -\sin \theta_e & -\sin(\theta_e - \frac{2\pi}{3}) & -\sin(\theta_e + \frac{2\pi}{3}) \\ \frac{1}{2} & \frac{1}{2} & \frac{1}{2} \end{bmatrix} \begin{bmatrix} i_{La} \\ i_{Lb} \\ i_{Lc} \end{bmatrix} \quad (3)$$

Since the  $dq$ -axis currents  $i_{Ld}$ ,  $i_{Lq}$  comprises the DC and AC current components, the DC current components  $\bar{i}_{Ld}$ ,  $\bar{i}_{Lq}$  of the  $dq$ -axis currents  $i_{Ld}$ ,  $i_{Lq}$  are extracted by using two second-order low pass filters [6]. The transfer function of the low pass filter is described as:

$$T(s) = \frac{k\omega^2}{s^2 + 2\zeta\omega s + \omega^2} \quad (4)$$

where the angular cut-off frequency  $\omega = 20\pi$  (rad/s), damping ratio  $\zeta = 0.7$ , and gain  $k = 1$ . The DC current component  $\bar{i}_{Ld}$  is added to the current  $i_{Cd}$  for generating the  $d$ -axis current command  $i_{Sd}^*$ . Additionally, the voltage difference between the DC-link voltage command  $V_{dc}^*$  and the DC-link voltage  $V_{dc}$  is transmitted to the DC-link controller, namely the PI, or the proposed WTSKFNN controller, for obtaining the control current  $i_{Cq}$ . Then, the summation of the DC current component  $\bar{i}_{Lq}$  and the control current  $i_{Cq}$  equals the  $q$ -axis current command  $i_{Sq}^*$ . The zero axis current  $i_{L0}$  is equal to the zero axis current command  $i_{S0}^*$ . The  $dq0$ -axis current commands  $i_{Sd}^*$ ,  $i_{Sq}^*$ ,  $i_{S0}^*$  are compared to the  $dq0$ -axis current  $i_{Sd}$ ,  $i_{Sq}$ ,  $i_{S0}$ , which are obtained by the grid currents  $i_{Sa}$ ,  $i_{Sb}$ ,  $i_{Sc}$  using the  $abc/dq0$  coordinate transformation, for acquiring the  $dq0$ -axis voltage commands  $v_d$ ,  $v_q$ ,  $v_0$ . The three

control commands  $v_{ca}$ ,  $v_{cb}$ ,  $v_{cc}$  can be computed via  $dq0/abc$  coordinate transformation in the following:

$$\begin{bmatrix} v_{ca} \\ v_{cb} \\ v_{cc} \end{bmatrix} = \begin{bmatrix} \cos \theta_e & -\sin \theta_e & 1 \\ \cos(\theta_e - \frac{2\pi}{3}) & -\sin(\theta_e - \frac{2\pi}{3}) & 1 \\ \cos(\theta_e + \frac{2\pi}{3}) & -\sin(\theta_e + \frac{2\pi}{3}) & 1 \end{bmatrix} \begin{bmatrix} v_d \\ v_q \\ v_0 \end{bmatrix} \tag{5}$$

The forth control command of the DSTATCOM can be obtained in the following:

$$v_{cn} = v_{ca} + v_{cb} + v_{cc} \tag{6}$$

At the final stage, the pulse width modulation (PWM) switching signals can be acquired to keep the constant DC-link voltage  $V_{dc}$  of the DSTATCOM, to suppress the current harmonics, neutral current, and three-phase unbalanced grid currents, and to compensate the reactive power for maintaining the unity of PF at the utility grid.

### 3. Intelligent WTSKFNN Controller

When the load varies, the instantaneous power follows into or out of the DC-link capacitor in the DSTATCOM, resulting in poor transient response and performance deterioration. Moreover, though the PI controller is extensively used due to the simple structure, the designed parameters of the PI controller are only for the assumed condition. In other words, the function of the PI controller is decreased in the case of an external disturbance such as sudden load change [19,20]. Consequently, to mend the transient responses of the grid currents and DC-link voltage and the performance of the DSTATCOM under load variation, the PI controller is substituted with the proposed WTSKFNN controller in this study. The network structure and online learning method of the proposed WTSKFNN are depicted as:

#### 3.1. Network Structure

The network structure of the developed WTSKFNN controller is illustrated in Figure 3. The proposed WTSKFNN comprises six layers, including the input layer (layer 1), membership layer (layer 2), rule layer (layer 3), TSK type fuzzy inference mechanism and wavelet layer (layer 4), consequent layer (layer 5), and output layer (layer 6). The detailed derivation of each layer is represented as follows:

##### 1. Input Layer:

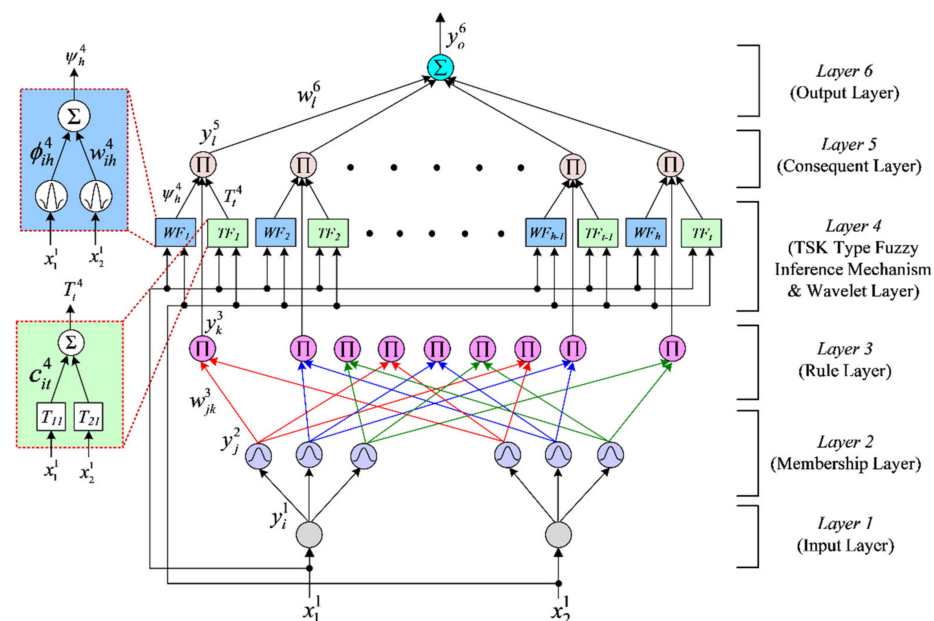


Figure 3. Network structure of WTSKFNN controller.

The relation of the node input and output is described as:

$$net_i^1(N) = x_i^1 \quad (7)$$

$$y_i^1(N) = f_i^1(net_i^1(N)) = net_i^1(N), i = 1, 2 \quad (8)$$

where  $x_i^1$  is the  $i$ th input to the input layer;  $N$  represents the  $N$ th iteration;  $x_1^1(N)$  is the DC-link voltage error  $e$ ; and  $x_2^1(N)$  is the derivative of DC-link voltage error  $\dot{e}$ .

## 2. Membership Layer:

To perform the fuzzification operation, the membership function adopts the Gaussian function in this study.

$$net_j^2(N) = -\frac{(y_i^1(N) - m_j^2(N))^2}{(\sigma_j^2(N))^2} \quad (9)$$

$$y_j^2(N) = f_j^2(net_j^2(N)) = \exp(net_j^2(N)) \quad (10)$$

$i = 1, j = 1, 2, 3$ , and  $i = 2, j = 4, 5, 6$

where  $\sigma_j^2(N)$  and  $m_j^2(N)$  are the standard deviation and the mean of the Gaussian function in the  $j$ th term associated with the  $i$ th input variable, respectively, and  $net_j^2(N)$  and  $y_j^2(N)$  are the input and the output of this layer.

## 3. Ruler Layer:

In rule layer, the multiplication operation is implemented in each node indicated by  $\Pi$ . The relationship of each node to multiply the input signals and output the result of product is described as:

$$net_k^3(N) = \Pi_j w_{jk}^3 y_j^2(N) \quad (11)$$

$$y_k^3(N) = f_k^3(net_k^3(N)) = net_k^3(N), k = 1, 2, \dots, 9 \quad (12)$$

where  $y_j^2(N)$  and  $y_k^3(N)$  are the input and output of rule layer;  $w_{jk}^3(N)$  is the connected weight between the rule layer and membership layer, and is set as 1.

## 4. TSK-Type Fuzzy Inference Mechanism and Wavelet layer:

The wavelet theory and the TSK-type fuzzy inference mechanism are carried out in this layer. The adopted wavelet theory is introduced as:

$$\phi_{ih}^4(N) = \frac{1}{\sqrt{|\sigma_{ih}^4|}} \left[ 1 - \frac{(x_i^1(N) - m_{ih}^4(N))^2}{(\sigma_{ih}^4)^2} \right] \exp \left[ -\frac{(x_i^1(N) - m_{ih}^4(N))^2}{2(\sigma_{ih}^4)^2} \right] \quad (13)$$

$i = 1, 2; h = 1, \dots, 9$

$$\psi_h^4 = \sum_i w_{ih}^4 \phi_{ih}^4(N), i = 1, 2; h = 1, \dots, 9 \quad (14)$$

where, the  $\phi_{ih}^4$  is  $i$ th in the  $h$ th term wavelet output to the node of wavelet sum layer;  $w_{ih}^4$  is the wavelet weight; and  $\psi_h^4(N)$  is the output of the wavelet theory. Moreover, a summation operation of the input variables is regarded as the output of the TSK type fuzzy inference mechanism. The relationship of each node  $t$  is described as follows:

$$T_t^4(N) = \sum_i c_{it}^4(N) x_i^1(N), i = 1, 2; t = 1, 2, \dots, 9 \quad (15)$$

where  $T_t^4(N)$  is the output of the TSK-type fuzzy inference mechanism and  $c_{it}^4(N)$  is the connected weight.

## 5. Consequent Layer:

In the consequent layer, the multiplication operation is adopted in each node expressed by  $\Pi$ . Each node multiplies the input variables  $y_k^3(N)$ ,  $\psi_h^4(N)$ ,  $T_t^4(N)$  and outputs the result of product  $y_l^5(N)$ .

$$net_l^5(N) = \prod_{h,t,k} \psi_h^4 T_t^4 y_k^3(N) \quad (16)$$

$$y_l^5(N) = f_l^5(net_l^5(N)) = net_l^5(N), l = 1, 2, \dots, 9 \quad (17)$$

#### 6. Output Layer:

The summation operation indicated by  $\Sigma$  is implemented in the output layer. The input and output of the node is expressed as:

$$net_o^6(N) = \sum_l w_l^6 y_l^5(N) \quad (18)$$

$$y_o^6(N) = f_o^6(net_o^6(N)) = net_o^6(N), o = 1 \quad (19)$$

where  $w_l^6$  is the connected weight between the consequent layer and the output layer. In this study, the output  $y_o^6(N)$  of this layer is equal to the control current  $i_{Cq}$ , as shown in Figure 2 for maintaining the constant DC-link voltage of the DSTATCOM under load variation.

#### 3.2. Online Learning Algorithm

The supervised learning algorithm is adopted to adjust the parameters in the proposed WTSKFNN controller online. The objective of the adjusted parameters in the proposed WTSKFNN controller using the backpropagation (BP) algorithm is to minimize a given error function. The error function  $E$  is represented as follows for the online learning algorithm:

$$E = \frac{1}{2} (V_{dc}^* - V_{dc})^2 = \frac{1}{2} e^2 \quad (20)$$

The update rules for the proposed WTSKFNN controller are detailed as follows:

#### 1. Output Layer:

In the output layer, the error term is derived as:

$$\delta_o^6 = -\frac{\partial E}{\partial y_o^6(N)} = -\frac{\partial E}{\partial V_{dc}} \frac{\partial V_{dc}}{\partial y_o^6(N)} \quad (21)$$

By means of chain rule algorithm, the connected weight  $w_l^6$  is calculated as:

$$\Delta w_l^6 = -\eta_1 \frac{\partial E}{\partial w_l^6(N)} = -\eta_1 \frac{\partial E}{\partial y_o^6(N)} \frac{\partial y_o^6(N)}{\partial w_l^6(N)} = \eta_1 \delta_o^6 y_l^5 \quad (22)$$

where  $\eta_1$  is the learning rate. Hence, the connected weight  $w_l^6$  will be updated as:

$$w_l^6(N+1) = w_l^6(N) + \Delta w_l^6 \quad (23)$$

#### 2. Consequent Layer:

The propagated error term of the consequent layer is described as:

$$\delta_l^5 = -\frac{\partial E}{\partial y_l^5(N)} = -\frac{\partial E}{\partial y_o^6(N)} \frac{\partial y_o^6(N)}{\partial y_l^5(N)} = \delta_o^6 w_l^6 \quad (24)$$

#### 3. TSK-Type Fuzzy Inference Mechanism and Wavelet Layer:

In this layer, two propagated error terms are derived as:

$$\delta_h^4 = -\frac{\partial E}{\partial \psi_h^4(N)} = -\frac{\partial E}{\partial y_l^5(N)} \frac{\partial y_l^5(N)}{\partial \psi_h^4(N)} = \delta_l^5 y_k^3 T_t^4 \quad (25)$$

$$\delta_t^4 = -\frac{\partial E}{\partial T_t^4(N)} = -\frac{\partial E}{\partial y_l^5(N)} \frac{\partial y_l^5(N)}{\partial T_t^4(N)} = \delta_l^5 y_k^3 \psi_h^4 \quad (26)$$

According to the BP algorithm, the updates of the wavelet weight  $\Delta w_{ih}^4$  and connected weight  $\Delta c_{it}^4(N)$  are depicted as:

$$\begin{aligned} \Delta w_{ih}^4 &= -\eta_2 \frac{\partial E}{\partial w_{ih}^4(N)} \\ &= -\eta_2 \frac{\partial E}{\partial y_l^5(N)} \frac{\partial y_l^5(N)}{\partial \psi_h^4(N)} \frac{\partial \psi_h^4(N)}{\partial w_{ih}^4(N)} = \begin{cases} \eta_2 \delta_h^4, \text{ the } \phi_{1t}^4, i = 1 \\ \eta_2 \delta_h^4, \text{ the } \phi_{2t}^4, i = 2 \end{cases} \end{aligned} \quad (27)$$

$$\begin{aligned} \Delta C_{it}^4 &= -\eta_3 \frac{\partial E}{\partial C_{it}^4(N)} \\ &= -\eta_3 \frac{\partial E}{\partial y_l^5(N)} \frac{\partial y_l^5(N)}{\partial T_t^4(N)} \frac{\partial T_t^4(N)}{\partial C_{it}^4(N)} = \begin{cases} \eta_3 \delta_t^4 x_1^1, i = 1 \\ \eta_3 \delta_t^4 x_2^1, i = 2 \end{cases} \end{aligned} \quad (28)$$

where  $\eta_2$  and  $\eta_3$  are learning rates. Thereupon, the wavelet weight  $\Delta w_{ih}^4$  and connected weight  $\Delta c_{it}^4(N)$  are updated and acquired as:

$$w_{ih}^4(N+1) = w_{ih}^4(N) + \Delta w_{ih}^4 \quad (29)$$

$$C_{it}^4(N+1) = C_{it}^4(N) + \Delta C_{it}^4 \quad (30)$$

#### 4. Ruler Layer:

The propagated error term in the rule layer is derived as:

$$\delta_k^3 = -\frac{\partial E}{\partial y_k^3(N)} = -\frac{\partial E}{\partial y_l^5(N)} \frac{\partial y_l^5(N)}{\partial y_k^3(N)} = \delta_l^5 \psi_h^4 T_t^4 \quad (31)$$

#### 5. Membership Layer:

In accordance with the chain rule algorithm, the error term is given as follows:

$$\delta_j^2 = -\frac{\partial E}{\partial \text{net}_j^2(N)} = -\frac{\partial E}{\partial y_k^3(N)} \frac{\partial y_k^3(N)}{\partial y_j^2(N)} \frac{\partial y_j^2(N)}{\partial \text{net}_j^2(N)} = \sum_k \delta_k^3 y_k^3 \quad (32)$$

The updated amount of the mean  $\Delta m_j^2$  and standard deviation  $\Delta \sigma_j^2$  of the membership functions are given as:

$$\begin{aligned} \Delta m_j^2 &= -\eta_4 \frac{\partial E}{\partial m_j^2} = -\eta_4 \frac{\partial E}{\partial y_k^3(N)} \frac{\partial y_k^3(N)}{\partial y_j^2(N)} \frac{\partial y_j^2(N)}{\partial \text{net}_j^2(N)} \frac{\partial \text{net}_j^2(N)}{\partial m_j^2(N)} \\ &= \eta_4 \delta_j^2 \frac{2(y_i^1 - m_j^2)}{(\sigma_j^2)^2} \end{aligned} \quad (33)$$

$$\begin{aligned} \Delta \sigma_j^2 &= -\eta_5 \frac{\partial E}{\partial \sigma_j^2} = -\eta_5 \frac{\partial E}{\partial y_k^3(N)} \frac{\partial y_k^3(N)}{\partial y_j^2(N)} \frac{\partial y_j^2(N)}{\partial \text{net}_j^2(N)} \frac{\partial \text{net}_j^2(N)}{\partial \sigma_j^2(N)} \\ &= \eta_5 \delta_j^2 \frac{2(y_i^1 - m_j^2)^2}{(\sigma_j^2)^2} \end{aligned} \quad (34)$$

where  $\eta_4$  and  $\eta_5$  are the learning rates of the mean and standard deviation, respectively. Thereupon, the mean  $m_j^2$  and standard deviation  $\sigma_j^2$  can be updated and acquired as follows:

$$m_j^2(N+1) = m_j^2(N) + \Delta m_j^2 \quad (35)$$

$$\sigma_j^2(N+1) = \sigma_j^2(N) + \Delta\sigma_j^2 \quad (36)$$

The precise calculation of the Jacobian of the VSC-based DSTATCOM,  $\partial V_{dc}/\partial y_o^6(N)$ , can't be resolved due to uncertainties such as external disturbances. Thus, for the purposes of overcoming this issue and increasing the online learning rates of the network parameters, the delta adaptation law is adopted as:

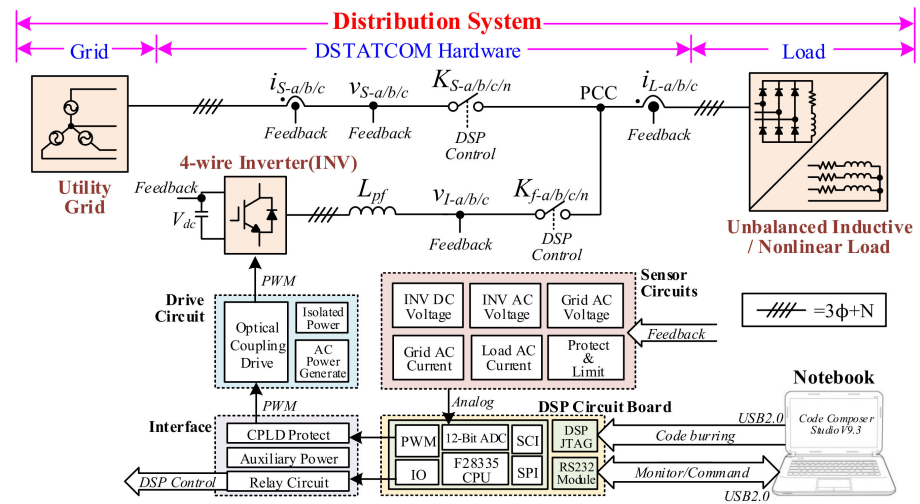
$$\delta_o^6 \cong e + \dot{e} \quad (37)$$

#### 4. Experimental Results

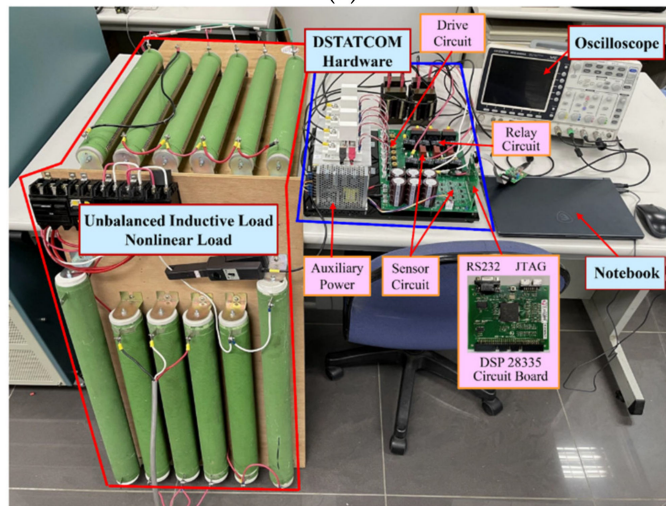
In this study, the digital signal processor (DSP)-based three-phase four-wire DSTATCOM platform is developed and illustrated in Figure 4. The hardware block diagram of the DSTATCOM in the distribution system is provided in Figure 4a. The three-phase grid voltages  $v_{Sa}$ ,  $v_{Sb}$ ,  $v_{Sc}$ , the grid currents  $i_{Sa}$ ,  $i_{Sb}$ ,  $i_{Sc}$ , the load currents  $i_{La}$ ,  $i_{Lb}$ ,  $i_{Lc}$ , and the DC-link voltage  $V_{dc}$  of the DSTATCOM are detected and sent to the analog-to-digital converter (ADC) for power quality enhancement. Moreover, the control algorithm comprising the intelligent WTSKFNN, PLL, DSTATCOM, and the DC-link voltage control are carried out through the TMS320F28335 DSP. The photo of the experimental setup is represented in Figure 4b. The specification of the DSP-based DSTATCOM is provided in Table 1. To verify the performance of the DSTATCOM using the proposed WTSKFNN controller for power quality enhancement, the three-phase unbalanced inductive loads 1 and 2 ( $R_{L-a,b,c}$ ,  $L_{L-a,b,c}$ ) are designed as shown in Table 1 to generate the three-phase unbalanced grid currents and the lagging PF. Nonlinear Loads 1 and 2 ( $R_{Ln}$ ,  $L_{Ln}$ ) will cause high THD of the grid current. Furthermore, Load *RL1* comprises the unbalanced inductive Load 1 and nonlinear Load 1. Load *RL2* is composed of the unbalanced inductive Load 2 and nonlinear Load 2. Load *RL3* consists of the Load *RL1* and Load *RL2*. Loads *RL1*, *RL2*, and *RL3* will cause deteriorated power quality. In addition, the unbalanced current ratio  $U_R$  is designed as follows to demonstrate the compensation performance of the three-phase unbalanced grid currents:

$$U_R = \frac{\text{Max}(i_{Sa}, i_{Sb}, i_{Sc}) - \text{Min}(i_{Sa}, i_{Sb}, i_{Sc})}{\text{Avg}(i_{Sa}, i_{Sb}, i_{Sc})} \quad (38)$$

where  $\text{Avg}(i_{Sa}, i_{Sb}, i_{Sc})$ ,  $\text{Max}(i_{Sa}, i_{Sb}, i_{Sc})$ , and  $\text{Min}(i_{Sa}, i_{Sb}, i_{Sc})$  depict the average current, the maximum current and the minimum current of the grid currents  $i_{Sa}$ ,  $i_{Sb}$ ,  $i_{Sc}$ , respectively. The lesser value the unbalanced current ratio  $U_R$  is, the better compensation performance the DSTATCOM owns. Additionally, to compare the performance of the DSTATCOM using the proposed WTSKFNN controller, the conventional PI and FNN controllers for DC-link voltage control as shown in Figure 2 are also adopted for demonstration.



(a)



(b)

**Figure 4.** DSP-based DSTATCOM platform. (a) Hardware block diagram of DSTATCOM in distribution system; (b) Photo of experimental setup.

**Table 1.** Specification of DSP-based DSTATCOM.

Symbol	Parameters	Values
$V_S$	System Voltage	220 Vrms(L-L), 60 Hz
$V_{dc}$	DC-Link Voltage	450 V
$C_{dc}$	DC-Link Capacitor	2820 $\mu$ F
$L_{pf}$	Interfacing Inductor	3 mH
$C_{pf}$	Ripple Filter	10 $\mu$ F
$f_{sw}$	Switching Frequency	18 kHz
$R_{L-a,b,c}, L_{L-a,b,c}$	Unbalanced Inductive Load 1	$R_{L_a}$ : 65 $\Omega$ , $L_{L_a}$ : 40 mH $R_{L_b}$ : 30 $\Omega$ , $L_{L_b}$ : 50 mH $R_{L_c}$ : 120 $\Omega$ , $L_{L_c}$ : 30 mH
	Unbalanced Inductive Load 2	$R_{L_a}$ : 20 $\Omega$ , $L_{L_a}$ : 50 mH $R_{L_b}$ : 10 $\Omega$ , $L_{L_b}$ : 30 mH $R_{L_c}$ : 50 $\Omega$ , $L_{L_c}$ : 40 mH
$R_{L_n}, L_{L_n}$	Nonlinear Load 1	75 $\Omega$ , 1 mH
	Nonlinear Load 2	50 $\Omega$ , 1 mH
$RL1$	Unbalanced Inductive Load 1 and Nonlinear Load 1	
$RL2$	Unbalanced Inductive Load 2 and Nonlinear Load 2	
$RL3$	$RL1$ and $RL2$	

Firstly, the scenario with the utility grid equipped with Load *RL2* is tested. The experimental result without using the DSTATCOM is shown in Figure 5. The response of the grid currents  $i_{Sa}$ ,  $i_{Sb}$ ,  $i_{Sc}$  and neural current  $i_{Sn}$  is provided in Figure 5a. The response of the phase-*a* grid voltage  $v_{Sa}$ , phase-*a* grid current  $i_{Sa}$ , and phase-*a* load current  $i_{La}$  is provided in Figure 5b. According to the experimental results shown in Figure 5, since the DSTATCOM is not adopted in the utility grid at Load *RL2*, the power quality is seriously deteriorated. The unbalanced current ratio  $U_R$ , the lagging PF, and the THD of the phase-*a* grid current are 53.38%, 0.895, and 18.23%, respectively. The RMS value of the neural current is 5.64 A. Moreover, the experimental result using the PI-controlled DSTATCOM is presented in Figure 6. The responses of the grid currents  $i_{Sa}$ ,  $i_{Sb}$ ,  $i_{Sc}$  and neural current  $i_{Sn}$  are shown in Figure 6a. The responses of the phase-*a* grid voltage  $v_{Sa}$ , phase-*a* grid current  $i_{Sa}$ , and phase-*a* load current  $i_{La}$  are represented in Figure 6b. The responses of the compensation currents  $i_{Fa}$ ,  $i_{Fb}$ ,  $i_{Fc}$  and DC-link voltage  $V_{dc}$  of the DSTATCOM are provided in Figure 6c. From the experimental results shown in Figure 6, since the compensation currents  $i_{Fa}$ ,  $i_{Fb}$ ,  $i_{Fc}$  of the DSTATCOM can suppress the current harmonics and unbalanced currents of the utility grid, and compensate the reactive power for maintaining the unity of PF, the power quality can be improved. The unbalanced current ratio  $U_R$ , the PF, and the THD of the phase-*a* grid current are 11.12%, 0.991, and 4.35%, respectively. The RMS value of the neural current is reduced to 1.14 A. In addition, the experimental results using the FNN-controlled DSTATCOM is illustrated in Figure 7. The responses of the grid currents  $i_{Sa}$ ,  $i_{Sb}$ ,  $i_{Sc}$  and neural current  $i_{Sn}$  are provided in Figure 7a. The responses of the phase-*a* grid voltage  $v_{Sa}$ , phase-*a* grid current  $i_{Sa}$ , and phase-*a* load current  $i_{La}$  are illustrated in Figure 7b. The responses of the compensation currents  $i_{Fa}$ ,  $i_{Fb}$ ,  $i_{Fc}$  and DC-link voltage  $V_{dc}$  of DSTATCOM are shown in Figure 7c. According to the experimental results using the FNN-controlled DSTATCOM, the unbalanced current ratio  $U_R$ , the PF, and the THD of the phase-*a* grid current are 8.05%, 0.997, and 4.02%, respectively. The RMS value of the neural current is reduced to 0.93 A. Hence, the power quality is slightly improved comparing to the PI-controlled DSTATCOM as shown in Figures 6 and 7. In addition, the experimental results using the proposed WTSKFNN-controlled DSTATCOM is provided in Figure 8. Since the proposed WTSKFNN comprises the WFNN and the TSK fuzzy control, the proposed WTSKFNN possesses the abilities in learning, converging quickly, parallel computation, and the capability to approximate nonlinear systems and uncertainties. Compared to the experimental results using PI- and FNN-controlled DSTATCOM, as shown in Figures 6 and 7, the power quality of the utility grid using the proposed WTSKFNN-controlled DSTATCOM is much improved, as shown in Figure 8. The unbalanced current ratio  $U_R$ , the PF, and the THD of the phase-*a* grid current are 5.15%, 0.998, and 3.71%, respectively. The RMS value of the neural current is much reduced, to 0.74 A. Additionally, the summary of the unbalanced current ratio  $U_R$ , PF, and THD of the three-phase grid currents at Load *RL1* and Load *RL2* is provided in Table 2. From the experimental results shown in Figures 5–8 and Table 2, the power quality enhancement can be achieved by using the proposed WTSKFNN-controlled DSTATCOM, owing to the robust and powerful capability of the proposed WTSKFNN controller.

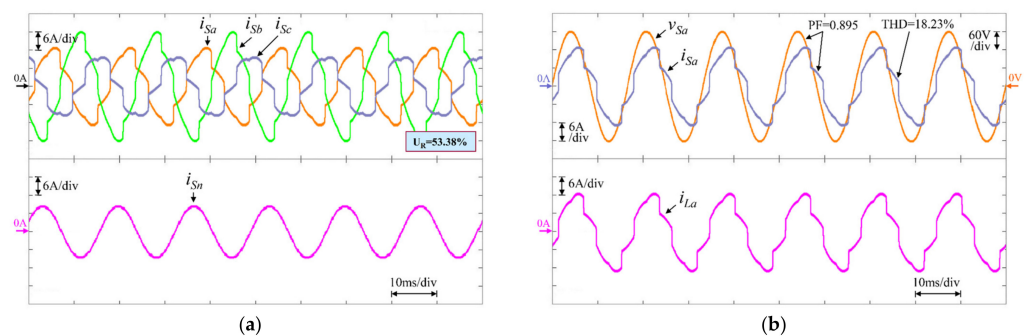


**Figure 5.** Experimental results without using DSTATCOM at RL2. (a) Response of grid currents and neural current; (b) Response of phase-*a* grid voltage, phase-*a* grid current, and phase-*a* load current.

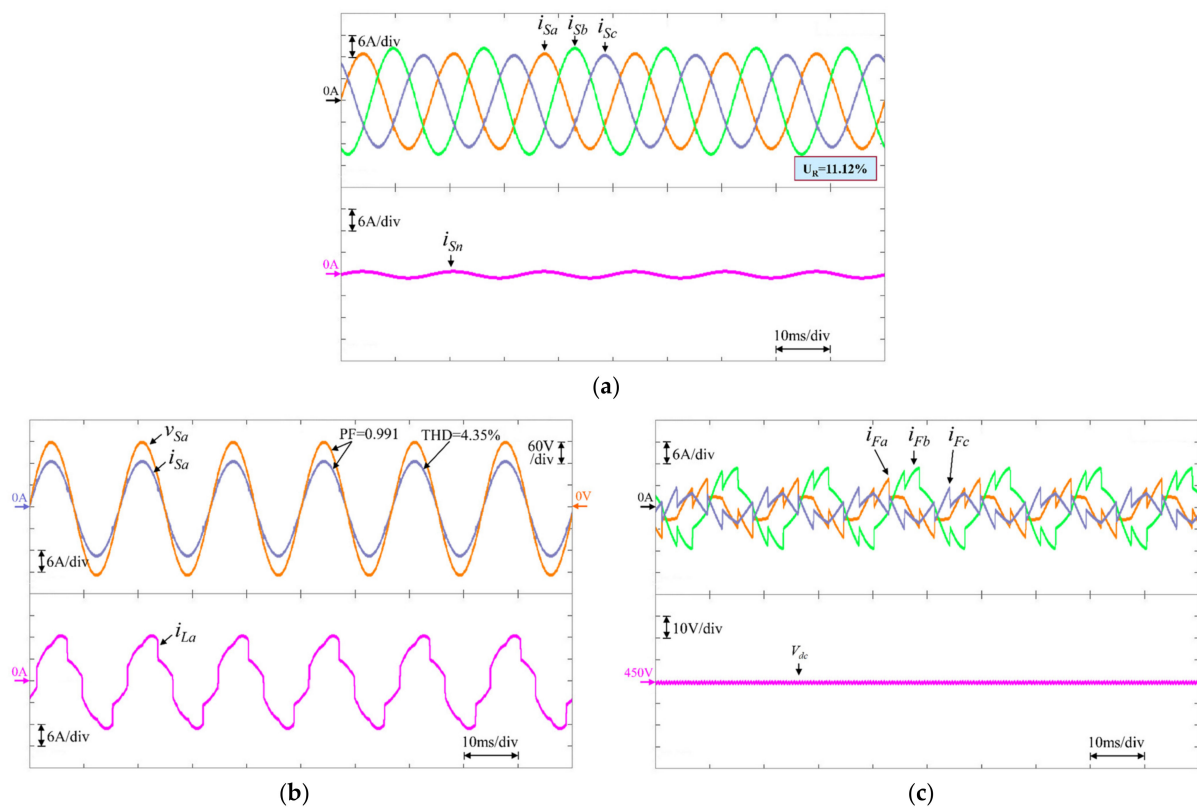


**Figure 6.** Experimental results using PI-controlled DSTATCOM at RL2. (a) Response of grid currents and neural current; (b) Response of phase-*a* grid voltage, phase-*a* grid current, and phase-*a* load current; and (c) Response of compensation currents and DC-link voltage of DSTATCOM.

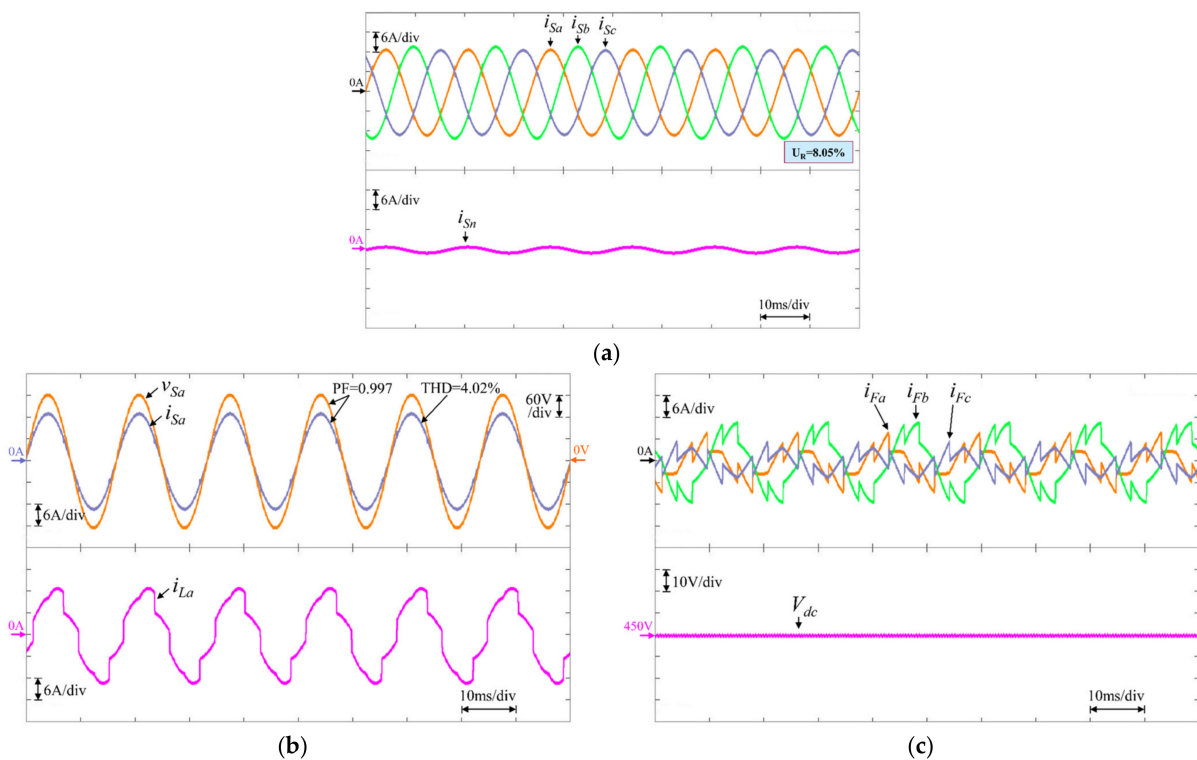


**Figure 7.** Experimental results using FNN-controlled DSTATCOM at RL2. (a) Response of grid currents and neural current; (b) Response of phase-*a* grid voltage, phase-*a* grid current, and phase-*a* load current; and (c) Response of compensation currents and DC-link voltage of DSTATCOM.

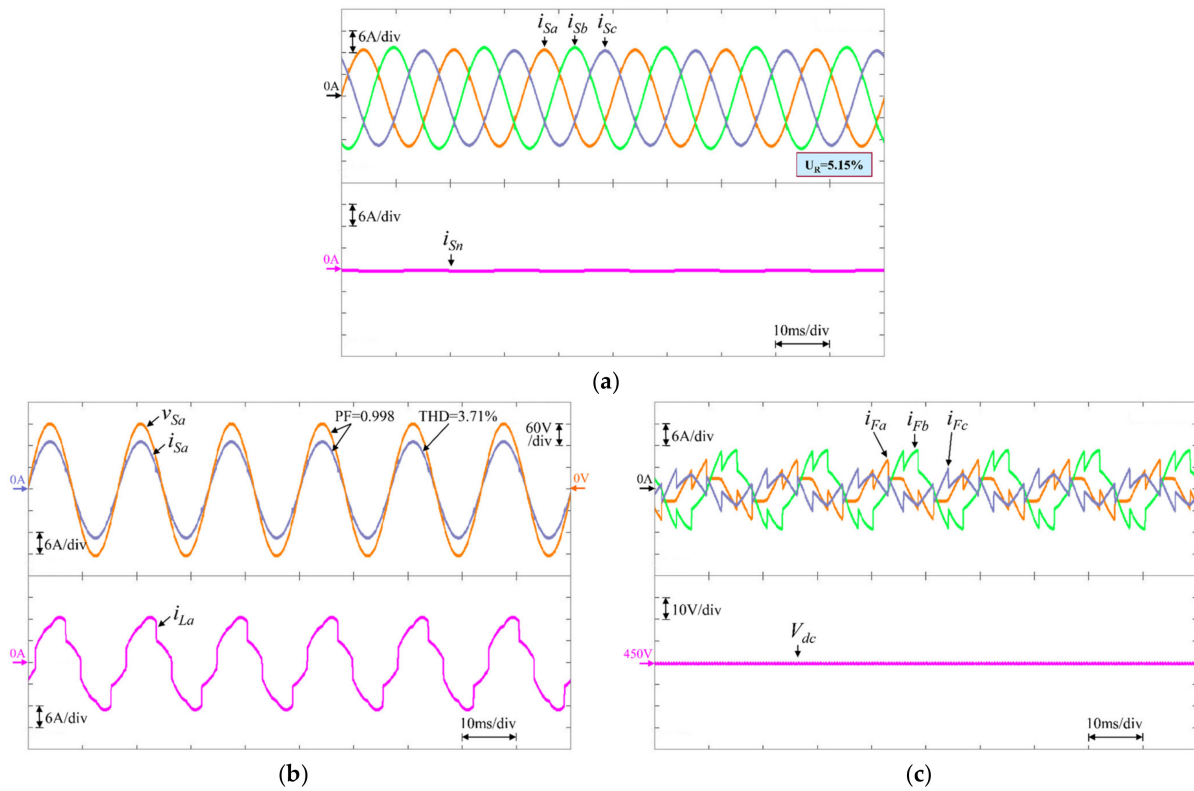


**Figure 8.** Experimental results using proposed WTSKFNN-controlled DSTATCOM at RL2. (a) Response of grid currents and neural current; (b) Response of phase-*a* grid voltage, phase-*a* grid current, and phase-*a* load current; and (c) Response of compensation currents and DC-link voltage of DSTATCOM.

**Table 2.** Summary of unbalanced current ratio, PF, and THD of three-phase grid currents at Load RL1 and Load RL2.

Type of Load	Strategy	$U_R$ (%)				THD (%)			Power Factor		
		$i_{S-a,b,c}$	$i_{Sa}$	$i_{Sb}$	$i_{Sc}$	$i_{Sa}$	$i_{Sb}$	$i_{Sc}$	$i_{Sa}$	$i_{Sb}$	$i_{Sc}$
RL1	Without Compensation	37.65	19.34	17.46	25.94	0.957	0.946	0.964			
	Traditional (PI)	12.57	4.34	4.38	4.39	0.996	0.997	0.996			
	FNN	9.44	3.91	4.05	4.01	0.997	0.997	0.998			
	WTSKFNN (Proposed)	5.71	3.67	3.74	3.71	0.998	0.997	0.998			
RL2	Without Compensation	53.38	18.23	12.68	23.46	0.895	0.834	0.954			
	Traditional (PI)	11.12	4.35	4.27	4.43	0.991	0.992	0.991			
	FNN	8.05	4.02	3.95	4.05	0.997	0.998	0.996			
	WTSKFNN (Proposed)	5.15	3.71	3.77	3.67	0.998	0.998	0.998			

Finally, two test scenarios under load variation are designed in the following: (1) Case 1: The load is changed from RL1 to RL3, and finally changed to RL2, and (2) Case 2: The load is changed from RL3 to RL1, and finally changed to RL2. The experimental results using the PI, FNN, and the proposed WTSKFNN-controlled DSTATCOM in Case 1 are represented in Figure 9. The responses of the grid currents and DC-link voltage of the PI-controlled DSTATCOM are shown in Figure 9a. The responses of the grid currents and DC-link voltage of the FNN-controlled DSTATCOM are represented in Figure 9b. The responses of the grid currents and DC-link voltage of the proposed WTSKFNN-controlled DSTATCOM are provided in Figure 9c. According to Figure 9a, since the parameters of the PI controller are unsuitable for the different conditions owing to poor disturbance rejection, the performance of the PI-controlled DSTATCOM is decreased during sudden load change. In other words, the transient responses of the grid currents  $i_{Sa}$ ,  $i_{Sb}$ ,  $i_{Sc}$  and DC-link voltage  $V_{dc}$  of the PI-

controlled DSTATCOM seriously fluctuate at the moment of sudden load change, resulting in the poor power quality. The response times of the grid currents and DC-link voltage during the load change are 1 s and 0.75 s. On the other hand, the transient responses of the grid currents  $i_{Sa}$ ,  $i_{Sb}$ ,  $i_{Sc}$  and DC-link voltage  $V_{dc}$  are improved by the FNN-controlled DSTATCOM at the moment of sudden load change as shown in Figure 9b. The response times of the grid currents and DC-link voltage during the load change are reduced to 0.3 s and 0.3 s, respectively. Moreover, compared to the PI- and FNN-controlled DSTATCOM, the transient responses of the grid currents  $i_{Sa}$ ,  $i_{Sb}$ ,  $i_{Sc}$  and DC-link voltage  $V_{dc}$  can be much improved by the proposed WTSKFNN-controlled DSTATCOM. The response times of the grid currents and DC-link voltage during the load change are much reduced, to 0.15 s and 0.12 s by the proposed WTSKFNN controller. In addition, the experimental results using the PI-, FNN-, and the proposed WTSKFNN-controlled DSTATCOM in Case 2 are illustrated in Figure 10. The power quality enhancement can also be achieved by using the proposed WTSKFNN-controlled DSTATCOM in Case 2. The transient responses of the grid currents  $i_{Sa}$ ,  $i_{Sb}$ ,  $i_{Sc}$  and DC-link voltage  $V_{dc}$  can also be much improved owing to the robust ability of the proposed WTSKFNN controller compared with the PI and FNN controller as shown in Figure 10. In other words, the DC-link voltage control can effectively maintain the constant voltage level under load variation by using the proposed WTSKFNN controller. Additionally, the response times of the grid currents and DC-link voltage error during the load change in Cases 1 and 2 are represented in Figure 11. In accordance with the experimental results shown in Figures 9–11, since the proposed WTSKFNN possesses the merits of the WFNN and TSK fuzzy control, the transient responses of the grid currents  $i_{Sa}$ ,  $i_{Sb}$ ,  $i_{Sc}$  and DC-link voltage  $V_{dc}$  under load variation can be much improved and achieve power quality enhancement.

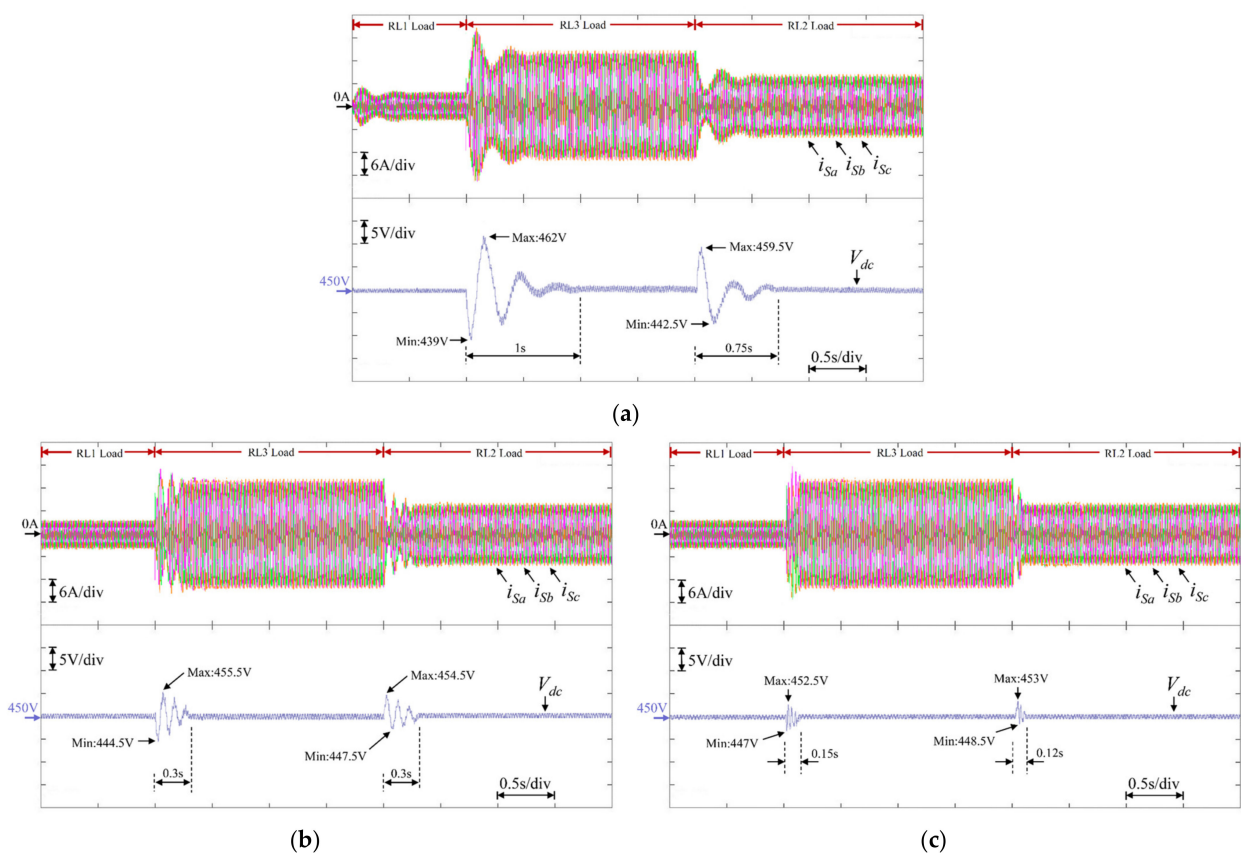


**Figure 9.** Experimental results under load variation in Case 1. (a) Response of grid currents and DC-link voltage of PI-controlled DSTATCOM; (b) Response of grid currents and DC-link voltage of FNN-controlled DSTATCOM; and (c) Response of grid currents and DC-link voltage of proposed WTSKFNN-controlled DSTATCOM.

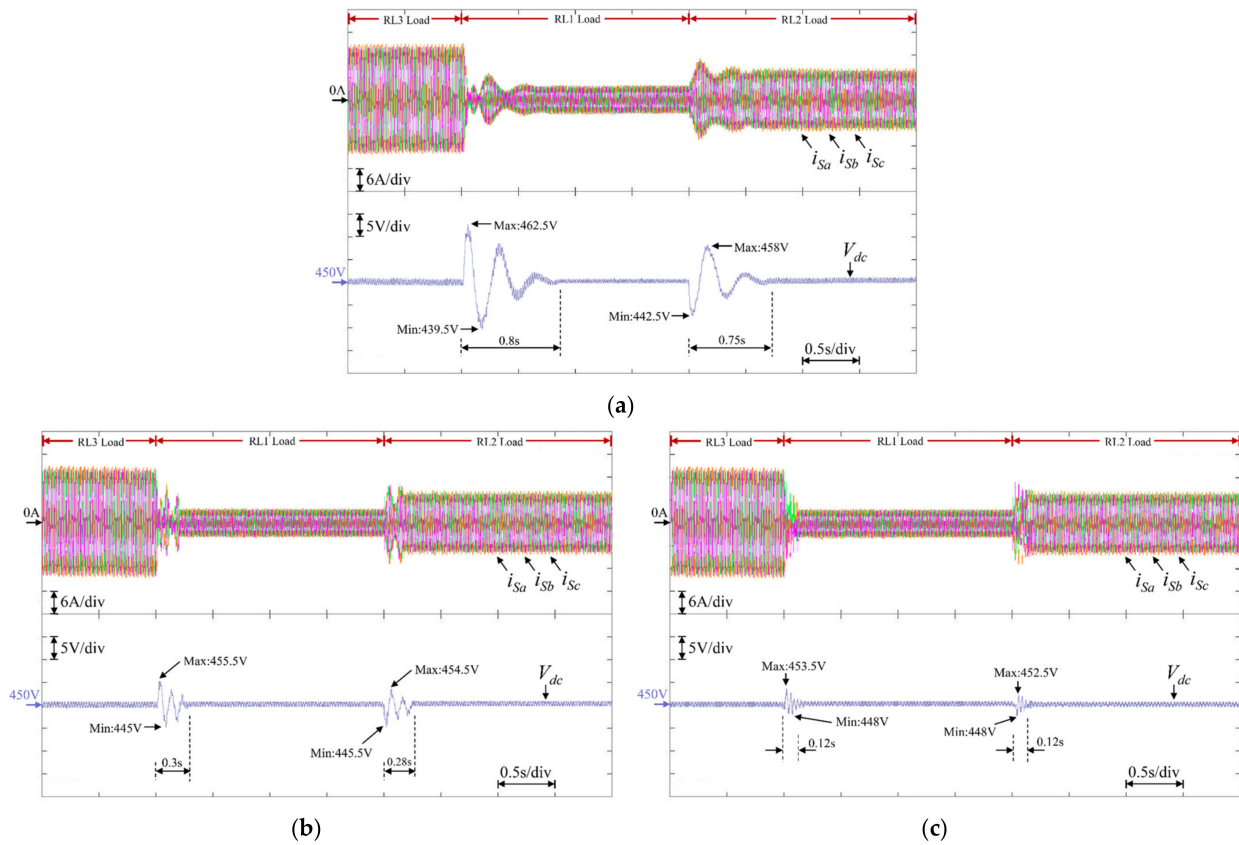


**Figure 10.** Experimental results under load variation in Case 2. (a) Response of grid currents and DC-link voltage of PI-controlled DSTATCOM; (b) Response of grid currents and DC-link voltage of FNN-controlled DSTATCOM; and (c) Response of grid currents and DC-link voltage of proposed WTSKFNN-controlled DSTATCOM.

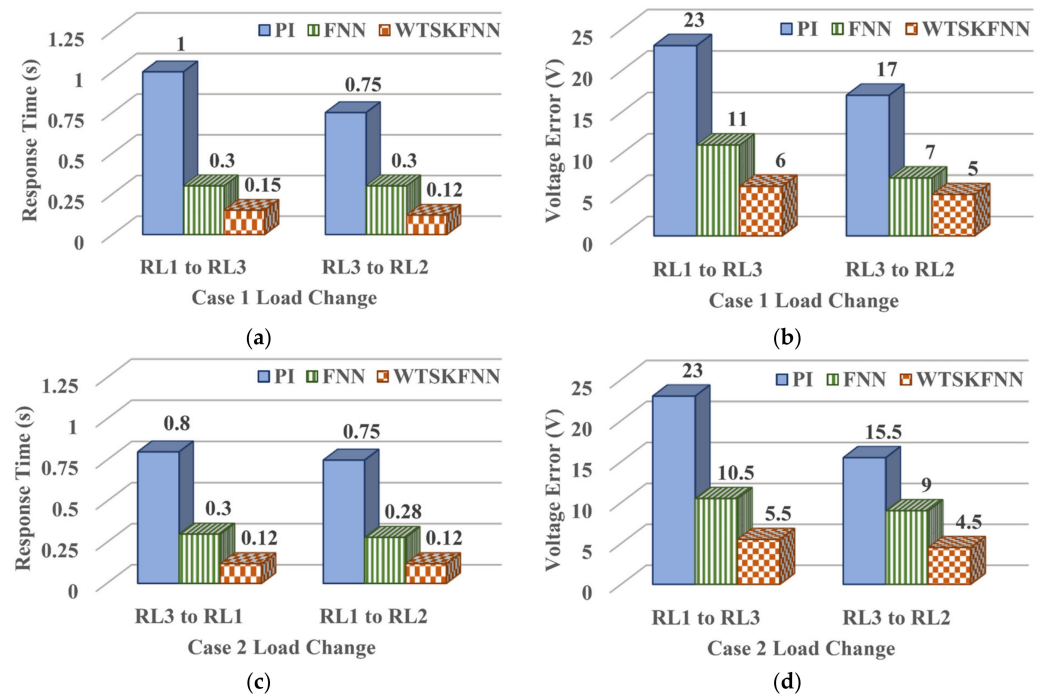


**Figure 11.** Transient response under load variation. (a) Response times of grid currents using different controller in Case 1; (b) DC-link voltage error of different controller in Case 1; (c) Response times of grid currents using different controller at Case 2; and (d) DC-link voltage error of different controller in Case 2.

The training or computation time of the “C” program in the DSP with 150 MHz is acquired by the clock tool of the Texas Instruments (TI) Code Composer Studio (CCS) v6 program editing interface in this study. The total computation time and the operation cycles of the PI-, FNN-, and the proposed WTSKFNN-controlled DSTATCOM are given in Table 3. The total computation time and the operation cycles for the proposed WTSKFNN are 0.1115 ms and 16,725 cycles, respectively. In consequence, the total execution time of the proposed WTSKFNN-controlled DSTATCOM is still less than 1 ms, which is the sampling time for the control loop.

**Table 3.** Computation time of DSTATCOM using PI, FNN, and proposed WTSKFNN controller.

Strategy	PI	FNN	Proposed WTSKFNN
Total Operation Cycles	1605	11,865	16,725
Execution Time	0.0107 ms	0.0791 ms	0.1115 ms

## 5. Conclusions

In this study, a three-phase four-wire DSTATCOM is proposed to enhance power quality. Since instantaneous power follows into or out of the DC-link capacitor in the DSTATCOM, poor transient response of the grid currents and DC-link voltage occurs under load variation. Moreover, to mend the transient response and the performance of the DSTATCOM, the traditional PI controller is substituted with the proposed WTSKFNN controller. According to the experimental results, the performance of the three-phase unbalanced grid currents compensation, the THD reduction, and the PF correction are much improved by using the proposed WTSKFNN-controlled DSTATCOM. In addition, the transient response of the grid currents and DC-link voltage under load variation are also much improved due to the powerful and robust ability of the WTSKFNN controller. Therefore, the main contributions of this study are: (i) the successful development of a three-phase four-wire DSTATCOM and the proposed WTSKFNN controller, and (ii) the successful application of the proposed WTSKFNN-controlled DSTATCOM for power quality enhancement.

**Author Contributions:** Conceptualization, J.-H.C. and K.-H.T.; methodology, J.-H.C. and K.-H.T.; software, J.-H.C.; validation, J.-H.C. and Y.-D.L.; formal analysis, J.-H.C. and K.-H.T.; investigation, K.-H.T. and Y.-D.L.; resources, J.-H.C.; data curation, Y.-D.L.; writing—original draft preparation, K.-H.T.; writing—review and editing, K.-H.T. and Y.-D.L. All authors have read and agreed to the published version of the manuscript.

**Funding:** This work was supported in part by the Ministry of Science and Technology of Taiwan, R.O.C., under grant MOST 109-2221-E-606-004-MY2 and in part by the Institute of Nuclear Energy Research, R.O.C., under grant 111A012.

**Institutional Review Board Statement:** Not applicable.

**Informed Consent Statement:** Not applicable.

**Data Availability Statement:** Not applicable.

**Conflicts of Interest:** The authors declare no conflict of interest.

## Nomenclature

$v_{Sa}, v_{Sb}, v_{Sc}$	Three-phase grid voltages.
$L_s, R_s$	Grid impedance.
$R_{Ln}, L_{Ln}$	Nonlinear load.
$R_{La}, L_{La}$	Phase- <i>a</i> unbalanced inductive load.
$R_{Lb}, L_{Lb}$	Phase- <i>b</i> unbalanced inductive load.
$R_{Lc}, L_{Lc}$	Phase- <i>c</i> unbalanced inductive load.
$C_{dc}$	DC-link capacitor.
$L_{pf}$	Interfacing Inductor.
$C_{pf}, R_{pf}$	Ripple Filter.
$i_{Fa}, i_{Fb}, i_{Fc}$	Three-phase compensation currents of DSTATCOM.

$i_{Fn}$	Four-wire compensation current of DSTATCOM.
$i_{La}, i_{Lb}, i_{Lc}$	Three-phase load currents.
$i_{Ld}, i_{Lq}, i_{L0}$	$dq0$ -axis load currents.
$\bar{i}_{Ld}, \bar{i}_{Lq}$	DC current components of the $dq$ -axis load currents.
$T(s)$	Transfer function of the low pass filter.
$\omega$	Angular cut-off frequency.
$\zeta$	Damping ratio.
$k$	Gain of the low pass filter.
$v_{Sd}$	$d$ -axis grid voltage.
$v_{Sd}^*$	$d$ -axis grid voltage command.
$\omega_e$	Electrical angular frequency.
$\theta_e$	Electrical angle.
$V_m$	Voltage amplitude of three-phase grid voltages.
$V_m^*$	Voltage amplitude command of three-phase grid voltages.
$i_{Cd}$	Voltage amplitude control current.
$V_{dc}$	DC-link voltage.
$V_{dc}^*$	DC-link voltage command.
$i_{Cq}$	DC-link control current.
$i_{Sd}^*$	$d$ -axis current command.
$i_{Sq}^*$	$q$ -axis current command.
$i_{S0}^*$	zero axis current command.
$i_{Sa}, i_{Sb}, i_{Sc}$	Three-phase grid currents.
$i_{Sd}, i_{Sq}, i_{S0}$	$dq0$ -axis grid currents.
$v_d, v_q, v_0$	$dq0$ -axis voltage commands.
$v_{ca}, v_{cb}, v_{cc}$	PWM switching signals of three-phase control commands.
$v_{cn}$	PWM switching signals of the forth control command.
$x_i^1$	Input of WTSKFNN.
$e$	DC-link voltage error.
$\dot{e}$	Derivative of DC-link voltage error.
$N$	Number of iterations.
$y_i^1$	Input linguistic variable to node of membership layer.
$\sigma_j^2$	Standard deviation of Gaussian function.
$m_j^2$	Mean of Gaussian function.
$y_j^2$	Output of membership layer.
$w_{jk}^3$	Connected weight between membership layer and rule layer.
$y_k^3$	Output of rule layer.
$WF_t$	Wavelet functions.
$\phi_{ih}^4$	$i$ th in the $h$ th term wavelet output to the node of wavelet sum layer.
$w_{ih}^4$	Connected weight of $WF_t$ layer.
$\psi_h^4$	Output of $WF_t$ layer.
$TF_h$	TSK type fuzzy inference mechanism functions.
$c_{it}^4$	Connected weight of $TF_h$ layer.
$T_t^4$	Output of $TF_h$ layer.
$y_l^5$	Output of consequent Layer.
$w_l^6$	Connected weight between consequent layer and output layer.
$y_o^6$	Output of WTSKFNN.
$E$	Energy function.
$\delta_o^6$	Error term of output layer.
$\delta_l^5$	Error term of consequent layer.
$\delta_h^4$	Error term of $TF_h$ layer.
$\delta_t^4$	Error term of $WF_t$ layer.
$\delta_k^3$	Error term of rule layer.
$\delta_j^2$	Error term of membership layer.
$\eta_1$	Learning rate of connected weight between consequent layer and output layer.
$\eta_2$	Learning rate of connected weight of $WF_t$ functions.
$\eta_3$	Learning rate of connected weight of $TF_h$ functions.
$\eta_4$	Learning rate of mean of Gaussian function.
$\eta_5$	Learning rate of standard deviation of Gaussian function.

## References

1. Lin, L.; He, J.; Xu, C. Analysis on circulating current and split capacitor voltage balance for modular multilevel converter based three-phase four-wire split capacitor DSTATCOM. *J. Mod. Power Syst. Clean Energy* **2021**, *9*, 657–667. [\[CrossRef\]](#)
2. Kumar, C.; Mishra, M.K.; Mekhilef, S. A new voltage control strategy to improve performance of DSTATCOM in electric grid. *CES Trans. Electr. Mach. Syst.* **2020**, *4*, 295–302. [\[CrossRef\]](#)
3. Xu, C.; Dai, K.; Chen, X.; Kang, Y. Unbalanced PCC voltage regulation with positive- and negative-sequence compensation tactics for MMC-DSTATCOM. *IET Power Electron.* **2016**, *9*, 2846–2858. [\[CrossRef\]](#)
4. Prasad, K.K.; Myneni, H.; Siva Kumar, G. Power quality improvement and PV power injection by DSTATCOM with variable DC link voltage control from RSC-MLC. *IEEE Trans. Sustain. Energy* **2019**, *10*, 876–885. [\[CrossRef\]](#)
5. Mishra, S.; Ray, P.K. Power quality improvement using photovoltaic fed DSTATCOM based on JAYA optimization. *IEEE Trans. Sustain. Energy* **2016**, *7*, 1672–1680. [\[CrossRef\]](#)
6. Pandu, S.B.; Sundarabalan, C.K.; Srinath, N.S.; Santhana Krishnan, T.; Soorya Priya, G.; Balasundar, C.; Sharma, J.; Soundarya, G.; Siano, P.; Alhelou, H.H. Power quality enhancement in sensitive local distribution grid using interval type-II fuzzy logic controlled DSTATCOM. *IEEE Access* **2021**, *9*, 59888–59899. [\[CrossRef\]](#)
7. Tan, K.H.; Lin, F.J.; Chen, J.H. DC-link voltage regulation using RPFNN-AMF for three-phase active power filter. *IEEE Access* **2018**, *6*, 37454–37463. [\[CrossRef\]](#)
8. Srinivas, M.; Hussain, I.; Singh, B. Combined LMS–LMF-based control algorithm of DSTATCOM for power quality enhancement in distribution system. *IEEE Trans. Ind. Electron.* **2016**, *63*, 4160–4168. [\[CrossRef\]](#)
9. Patel, S.K.; Arya, S.R.; Maurya, R. Nonlinear adaptive volterra filter for control of distribution static compensator. *IEEE J. Emerg. Sel. Top. Power Electron.* **2017**, *5*, 559–567. [\[CrossRef\]](#)
10. Patel, S.K.; Arya, S.R.; Maurya, R.; Babu, B.C. Control scheme for DSTATCOM based on frequency-adaptive disturbance observer. *IEEE J. Emerg. Sel. Top. Power Electron.* **2018**, *6*, 1345–1354. [\[CrossRef\]](#)
11. Singh, B.; Solanki, J. A comparison of control algorithms for DSTATCOM. *IEEE Trans. Ind. Electron.* **2009**, *56*, 2738–2745. [\[CrossRef\]](#)
12. Czarnecki, L.S. Instantaneous reactive power p-q theory and power properties of three-phase systems. *IEEE Trans. Power Deliv.* **2006**, *21*, 362–367. [\[CrossRef\]](#)
13. Freitas, W.; Morelato, A.; Xu, W.; Sato, F. Impacts of AC generators and DSTATCOM devices on the dynamic performance of distribution systems. *IEEE Trans. Power Deliv.* **2005**, *20*, 1493–1501. [\[CrossRef\]](#)
14. Singh, B.; Jayaprakash, P.; Kothari, D.P. A t-connected transformer and three-leg VSC based DSTATCOM for power quality improvement. *IEEE Trans. Power Electron.* **2008**, *23*, 2710–2718. [\[CrossRef\]](#)
15. Bagheri, M.; Nurmanova, V.; Abedinia, O.; Naderi, M.S. Enhancing power quality in microgrids with a new online control strategy for DSTATCOM using reinforcement learning algorithm. *IEEE Access* **2018**, *6*, 38986–38996. [\[CrossRef\]](#)
16. Kumar, A.; Kumar, P. Power quality improvement for grid-connected PV system based on distribution static compensator with fuzzy logic controller and UVT/ADALINE-based least mean square controller. *J. Mod. Power Syst. Clean Energy* **2021**, *9*, 1289–1299. [\[CrossRef\]](#)
17. Chawda, G.S.; Shaik, A.G. Enhancement of wind energy penetration levels in rural grid using ADALINE-LMS controlled distribution static compensator. *IEEE Trans. Sustain. Energy* **2022**, *13*, 135–145. [\[CrossRef\]](#)
18. Khoshooei, A.; Moghani, J.S.; Candela, I.; Rodriguez, P. Control of D-STATCOM during unbalanced grid faults based on DC voltage oscillations and peak current limitations. *IEEE Trans. Ind. Appl.* **2018**, *54*, 1680–1690. [\[CrossRef\]](#)
19. Zhou, X.; Zhong, W.; Ma, Y.; Guo, K.; Yin, J.; Wei, C. Control strategy research of D-STATCOM using active disturbance rejection control based on total disturbance error compensation. *IEEE Access* **2021**, *9*, 50138–50150. [\[CrossRef\]](#)
20. Woo, J.H.; Wu, L.; Lee, S.M.; Park, J.B.; Roh, J.H. D-STATCOM d-q axis current reference control applying DDPG algorithm in the distribution system. *IEEE Access* **2021**, *9*, 145840–145851. [\[CrossRef\]](#)
21. Tan, K.H. Squirrel cage induction generator system using wavelet petri fuzzy neural network control for wind power applications. *IEEE Trans. Power Electron.* **2016**, *31*, 5242–5254. [\[CrossRef\]](#)
22. Lin, F.J.; Hung, Y.C.; Ruan, K.C. An intelligent second-order sliding-mode control for an electric power steering system using a wavelet fuzzy neural network. *IEEE Trans. Fuzzy Syst.* **2014**, *22*, 1598–1611. [\[CrossRef\]](#)
23. Yilmaz, S.; Oysal, Y. Fuzzy wavelet neural network models for prediction and identification of dynamical systems. *IEEE Trans. Neural Netw.* **2010**, *21*, 1599–1609. [\[CrossRef\]](#)
24. Lin, F.J.; Tan, K.H.; Luo, W.C.; Xiao, G.D. Improved LVRT performance of PV power plant using recurrent wavelet fuzzy neural network control for weak grid conditions. *IEEE Access* **2020**, *8*, 69346–69358. [\[CrossRef\]](#)
25. El-Sousy, F.F.M.; Amin, M.M.; Mohammed, O.A. Robust optimal control of high-speed permanent-magnet synchronous motor drives via self-constructing fuzzy wavelet neural network. *IEEE Trans. Ind. Appl.* **2021**, *57*, 999–1013. [\[CrossRef\]](#)
26. Lin, F.J.; Liao, J.C.; Chen, C.I.; Chen, P.R.; Zhang, Y.M. Voltage restoration control for microgrid with recurrent wavelet petri fuzzy neural network. *IEEE Access* **2022**, *10*, 12510–12529. [\[CrossRef\]](#)
27. Qin, B.; Nojima, Y.; Ishibuchi, H.; Wang, S. Realizing deep high-order TSK fuzzy classifier by ensembling interpretable zero-order TSK fuzzy subclassifiers. *IEEE Trans. Fuzzy Syst.* **2021**, *29*, 3441–3455. [\[CrossRef\]](#)
28. Lin, F.J.; Lu, K.C.; Ke, T.H.; Yang, B.H.; Chang, Y.R. Reactive power control of three-phase grid-connected PV system during grid faults using Takagi–Sugeno–Kang probabilistic fuzzy neural network control. *IEEE Trans. Ind. Electron.* **2015**, *62*, 5516–5528. [\[CrossRef\]](#)

29. Yen, J.; Wang, L.; Gillespie, C.W. Improving the interpretability of TSK fuzzy models by combining global learning and local learning. *IEEE Trans. Fuzzy Syst.* **1998**, *6*, 530–537. [[CrossRef](#)]
30. Lin, F.J.; Hung, Y.C.; Tsai, M.T. Fault-tolerant control for six-phase PMSM drive system via intelligent complementary sliding-mode control using TSKFNN-AMF. *IEEE Trans. Ind. Electron.* **2013**, *60*, 5747–5762. [[CrossRef](#)]
31. Zhang, T.; Deng, Z.; Ishibuchi, H.; Pang, L.M. Robust TSK fuzzy system based on semisupervised learning for label noise data. *IEEE Trans. Fuzzy Syst.* **2021**, *29*, 2145–2157. [[CrossRef](#)]